An original growth mode of MWCNTs on alumina supported iron catalysts

Régis Philippe [a,b,c], Brigitte Caussat [c], Andrea Falqui [d], Yolande Kihn [e], Philippe Kalck [a,b], Serge Bordère [f], Dominique Plee [f], Patrice Gaillard [f], Daniel Bernard [g], Philippe Serp [a,b,*]

[a] CNRS, Laboratoire de Chimie de Coordination – Composante ENSIACET, 205, route de Narbonne, F-31077 Toulouse, France
[b] Université de Toulouse, UPS, INPT, LCC, F-31077 Toulouse, France
[c] Laboratoire de Génie Chimique, École Nationale Supérieure des Ingénieurs en Arts Chimiques et Technologiques, UMR CNRS 5503, 5 rue Paulin Talabot, BP 1301, 31106 Toulouse Cedex 1, France
[d] Electron Microscopy Laboratory, Istituto Italiano di Tecnologia, Via Morego 30, Genova, Italy
[e] Centre d'Élaboration des Matériaux et d'Études Structurales, UPR CNRS 8011, 29 rue Jeanne Marvig, 31055 Toulouse, France
[f] ARKEMA, Groupement de Recherches de Lacq, BP 34, 64170 Lacq, France
[g] ARKEMA, 420 rue Estiennes d'Orves, 92700 Colombes, France

Multi-walled carbon nanotubes (MWCNTs) have been produced from ethylene by fluidized bed-catalytic chemical vapor deposition (FB-CCVD) on alumina supported iron catalyst powders. Both catalysts and MWCNTs-catalyst composites have been characterized by XRD, SEM-EDX, TEM, Mössbauer spectroscopy, TGA and nitrogen adsorption measurements at different stages of the process. The fresh catalyst is an alumina/iron oxide powder composed of amorphous iron(III) oxide nanoparticles located inside the porosity of the alumina support and of a micrometric crystalline α-iron(III) oxide surface film. The beginning of the CVD process provokes a brutal reconstruction and simultaneous carburization of the surface film that allows MWCNT nucleation and growth. These MWCNTs grow aligned between the support and the surface catalytic film, leading to a uniform consumption and uprising of the film. When the catalytic film has been consumed, the catalytic particles located inside the alumina porosity are slowly reduced and activated leading to a secondary MWCNT growth regime, which produces a generalized grain fragmentation and entangled MWCNT growth. Based on experimental observations and characterizations, this original two-stage growth mode is discussed and a general growth mechanism is proposed.

1. Introduction

Due to their outstanding physico-chemical properties and their unique morphology [1,2], during the last two decades MWCNTs have received much attention from both the scientific and industrial communities. Besides the key issue of safety and environmental impact, it is necessary to synthesize these new materials on a significant scale in order to improve their availability for the still growing number of potential applications, and to see their prices decrease on the market place. Among the numerous existing synthesis processes [3], FB-CCVD appears to be the most promising route to achieve this objective because of its cheapness, flexibility, high yield, homogeneity and selectivity [4]. Today, bottlenecks are still remaining like the control of CNT morphology and the improvement of CNT dispersion in different media that limit the optimal development of some applications like composite materials.

In order to improve the morphology control, a detailed knowledge of catalyst structure and CNT growth mode is essential. If the studies dealing with CNT growth are relatively numerous in the literature [3,5–7], the various experimental observations often lead to different approaches to explain the peculiar growth modes of these materials. Thus, some aspects of CNT growth are still poorly understood and need further studies, for example:

- Nanoparticles that act as catalyst but also template are often described to be necessary to produce MWCNTs, but on the other hand, particles with mean diameters larger than those (internal or external) of the formed tubes are also reported as efficient [8,9];
- Based on the metal–support interaction and shape considerations, MWCNT growth can involve tip-growth or base-growth mechanism [6] or a combination of the two [10];
- Finally, some authors described the growth as resulting from carbon diffusion through a bulk Fe₃C nanoparticle (bulk diffu-

sion) [6] while others think that it is only a surface Fe_3C film at the top of the particle that conducts the growth (surface diffusion) [11,12].

These observations illustrate the diversity of growth modes and underline the necessity to carefully characterize each new CNT synthesis catalyst in order to understand the growth mode.

As far as the dispersion of CNTs is concerned, the large scale controlled growth of vertically aligned CNTs may contribute to solve the problems encountered in this area, since this growth type permits the control of the CNT length. The growth of aligned MWCNTs has been first reported in 1996 [13] on flat substrates. Since this discovery, this field of investigation has known a great interest, especially for the development of field emitter's displays [14] or catalyst supports [15]. When we started this work, no article in the open and patented literature was dealing with the large scale synthesis of uniform and vertically aligned MWCNTs on a catalytic powder. Since then, only scarce studies have reported the synthesis of this type of material [16–18] by using the floating catalyst method, which normally involves discrete nanoparticles. Up to now, there is still a lack concerning catalytic systems characterization, which could provide valuable information on the growth mode of these materials.

In this work we present the characterization of an alumina supported iron catalyst, prepared by organometallic chemical vapor deposition, before and during the synthesis of MWCNTs by FB-CCVD. During the first stage of the process vertically aligned MWCNTs are produced from primary catalytic sites, whereas entangled MWCNTs are produced in a second stage from secondary catalytic sites. The main objective of this study was to understand the phenomena involved so as to explain how this catalyst operates. More generally, this work may contribute to the development of a catalytic system allowing mass-production of aligned MWCNTs with a controlled length.

2. Experimental

2.1. Catalyst preparation

The Fe/Al_2O_3 catalysts used in this study were prepared by low pressure fluidized bed organometallic chemical vapor deposition (OMCVD) in a specially designed vessel described elsewhere [19]. The support used was a commercial pseudo-boehmite alumina (SASOL, 204 m^2/g, mean volume diameter of 322 μm, minimum fluidization velocity U_{mf} at 650 °C of 3.5 cm/s), and the iron precursor was ferrocene (Strem Chemicals, 98% of purity). A low partial pressure of air was introduced during the chemical vapor deposition experiments to assist the decomposition of the precursor into iron oxide. The solid ferrocene precursor was firstly sublimed at 110 °C and then decomposed in the fluidized bed of alumina grains at 575 °C using nitrogen as carrier gas and air as reactive gas. The pressure in the reactor was kept at 80 Torr. The metal loading of the as-prepared catalysts, determined by inductively coupled plasma (ICP), was found to be of 10.15% (w/w).

2.2. Carbon nanotubes synthesis

Carbon nanotubes were synthesized by atmospheric FB-CCVD in a reactor entirely constructed in 304L stainless steel; its dimensions being 5.3 cm internal diameter and 1 m height (heated zone). The gas distributor was a stainless steel grid supplied with 50 μm holes. A multi-zone electrical furnace allowed monitoring of the bed temperature via several thermocouples (one by zone) fixed on the outer wall of the reactor. Temperature at three levels in the fluidized bed was registered through thermocouples placed along the reactor axis. Electronic grade ethylene, hydrogen and nitrogen gases (Air Liquide) were supplied to the reactor through mass-flow-meters. A pressure sensor allowed measuring the differential pressure drop between the bottom and the top of the reactor. After their exit from the reactor, the gaseous effluents flowed through a bag filter, in order to collect elutriated particles or fines that could be formed. An online gas chromatograph coupled with an automatic injection loop allowed the qualitative and quantitative analysis of the gaseous effluents before flowing by the outlet. The experimental set up is shown in Fig. 1a.

2.3. Experimental protocol for CNT growth

For all the experiments conducted in this study, the initial mass of catalyst bed was constant and equal to 60 g leading to an initial fixed-bed height of 3 cm. The total volumetric flow was maintained to 5330 sccm (standard cubic centimeters per minute) ensuring a gaseous velocity equal to 4 times the velocity at the minimum of fluidization at 650 °C (2.9 times at 400 °C). In order to obtain comparable successive points for characterization, the same following five-step protocol was used and only the time of carbon deposition varied from 1 s (pulse experiment) to 120 min. Before detailing the protocol, it must be noted that the first three steps, which permit reaching 650 °C, were not all of them performed under a reductive atmosphere. Indeed, if hydrogen is introduced during step 3, we noticed a rough defluidization of the bed that might be due to too high interparticles interactions during this high temperature type reduction:

- The first step consisted in the regular heating of the fluidized bed during 30 min until stabilization at 400 °C and occurs under an atmosphere composed of 50% nitrogen and 50% hydrogen.
- The second step was a reductive plateau of 60 min at 400 °C under the same atmosphere and gas velocity.
- The third step consisted in a second regular heating during 30 min from 400 °C until stabilization at 650 °C under pure nitrogen.
- The fourth step was the deposition plateau that occurs at a constant temperature of 650 °C under an atmosphere composed of 25% nitrogen, 25% hydrogen and 50% ethylene.
- The fifth and last step consisted in the natural cooling of the bed under pure nitrogen until the bed temperature reaches the ambient.

The synthesis protocol is schematized in Fig. 1b. The 9 points appearing on this figure illustrate the selected moments chosen for catalyst characterizations. They are further described in Table 1.

2.4. Characterization of the catalyst and catalyst–MWCNT composites

XRD patterns were recorded at room temperature with a SEIFERT XRD 3000 spectrometer using CuKα radiation (1.54 Å). The scans were recorded in the 2θ range between 20° and 80° using a step size of 0.05°. Peaks were identified by comparison with standards in the Joint Committee on Powder Diffraction Standards (JCPDS) database. Mössbauer spectroscopy was used to follow the evolution of the nature and structure of the iron catalyst. A constant-acceleration Mössbauer spectrometer using a 25 mCi ^{57}Co in Rh matrix was used at −190 °C. Responses were identified by comparison with literature data. Scanning electron microscopy (SEM) observations were performed with a Leo-435 microscope; products were analyzed with and without grinding and when necessary, EDX and X-ray cartographies measurements were performed. Field effect SEM (FE-SEM) observations were performed on a Hitachi S4500I. Transmission electron microscope (TEM) ob-
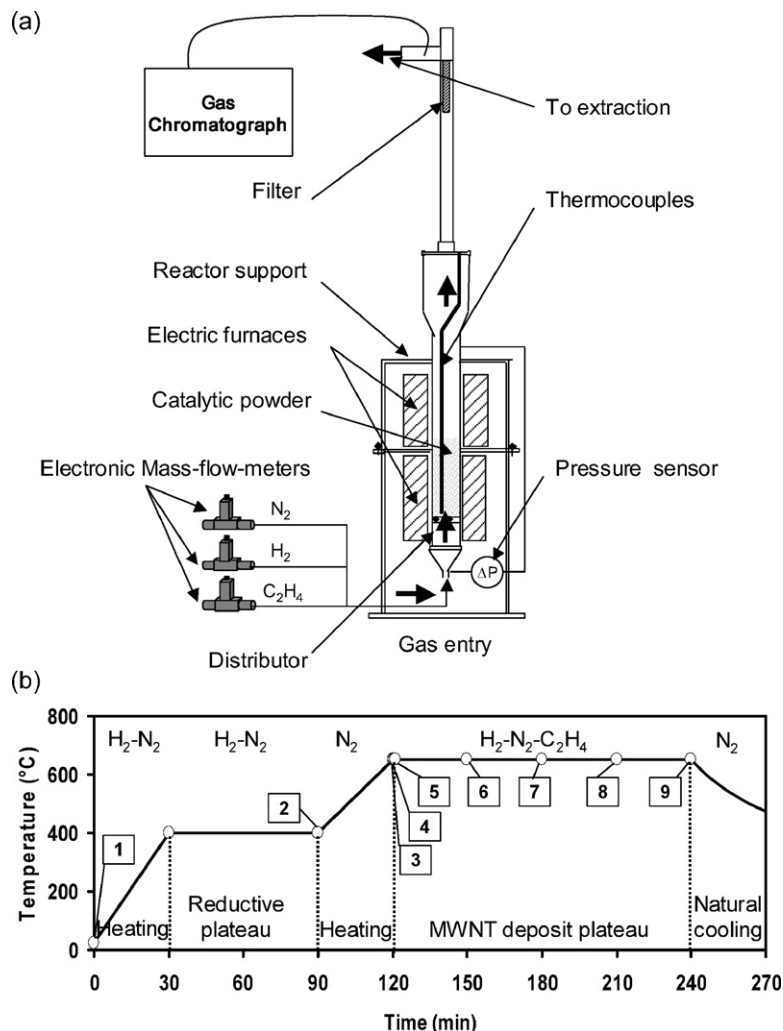
Fig. 1. (a) Experimental set-up; and (b) detailed MWCNT synthesis route and selected points for the characterizations of the catalyst.

Steps	Description of the material
1	As-prepared catalyst
2	Catalyst after the first heating and the 60 min reductive plateau at 400 °C under H_2–N_2
3	Catalyst after the heating to 650 °C under N_2
4	Composite material catalyst/CNT after 1 s (pulse experiment) of carbon deposit under H_2–N_2–C_2H_4
5	Composite material catalyst/CNT after 60 s of carbon deposit under H_2–N_2–C_2H_4
6	Composite material catalyst/CNT after 30 min of carbon deposit under H_2–N_2–C_2H_4
7	Composite material catalyst/CNT after 60 min of carbon deposit under H_2–N_2–C_2H_4
8	Composite material catalyst/CNT after 90 min of carbon deposit under H_2–N_2–C_2H_4
9	Composite material catalyst/CNT after 120 min of carbon deposit under H_2–N_2–C_2H_4

servations at low and high magnification were obtained using a Philips CM-12 microscope operating at 120 kV and having a resolving power of 3 Å. When desired, the samples were purified with hot sulfuric acid in order to remove the alumina support and most of the iron. Then, systematically, the samples were put in absolute ethyl alcohol and exposed to an ultrasonic bath to obtain a good dispersion.

The high resolution transmission electron microscopy (HRTEM) analysis was carried out by a Jeol 2100F microscope, equipped with ultra high resolution pole piece, field emission Schottky electron source and operating at 200 kV. One HRTEM image is reported, together with the bi-dimensional fast Fourier transform (2D-FFT) of the area indicated with a square in the HRTEM image.

Thermo-gravimetric analysis (TGA) measurements were conducted on a Setaram thermobalance in which the sample is heated in air from 25 to 1000 °C at a rate of 10 °C/min and followed by a 30 min isotherm at the final temperature. Nitrogen adsorption-desorption analyses were performed using a Micromeritics 2010 equipment, so as to obtain the BET specific surface area and information concerning the porosity of the powders. The distribution of grain diameters was measured with a Malvern Mastersizer Sirocco 2000 laser granulometer.

3. Results and discussion

3.1. Starting point: macroscopic observations

During the kinetic study performed on our system [20], we had noticed that the mean particle size of the manufactured composite powder (CNTs + catalyst) increases at a constant rate with deposition time. As shown in Fig. 2, this phenomenon lasted for 90 min of reaction. After that, the mean particle size decreased, indicating a generalized grain fragmentation, a phenomenon already reported for MWCNT growth on active catalysts [21]. SEM
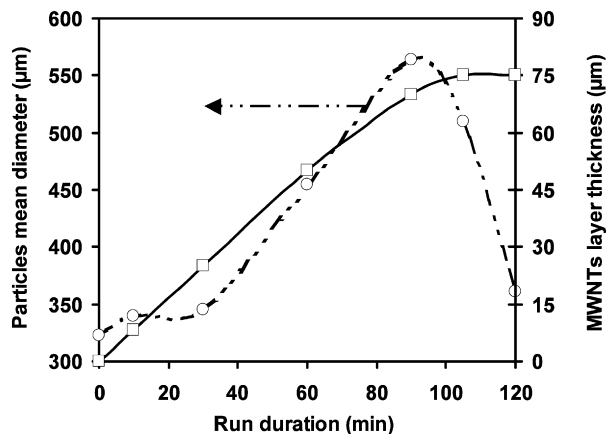
Fig. 2. Evolution with run duration (left side) of particles mean diameter and the average thickness of MWCNT mat (right side).

Table 2
Mössbauer parameters of the catalyst at different steps of the process.

Steps	Signals	δ (mm/s)	Δ (mm/s)	H (kOe)	R (%)	Attribution
1	D_1	0.39	1.03	–	78.12	Fe(III)
	S_1	0.48	–	536.0	21.88	Fe(III) super-paramagnetic
2	D_1	0.39	0.86	–	57.52	Fe(III)
	D_2	0.83	2.20	–	26.67	Fe(II)
	S_2	0.003	–	330.4	15.81	Fe(0)
3	D_1	0.46	1.06	–	53.10	Fe(III)
	D_2	1.05	0.46	–	34.25	Fe(II) sites of Fe_3O_4 and other Fe(II)
	S_1	0.12	–	337.6	7.16	Fe(0)
	S_3	0.59	–	501.8	5.48	Fe(III) sites of Fe_3O_4
4	D_1	0.46	0.94	–	50.02	Fe(III)
	D_2	1.04	2.73	–	36.61	Fe(II)
	S_4	0.30	–	244.6	13.37	Fe_3C
5	D_1	0.32	1.19	–	47.32	Fe(III)
	D_2	1.19	2.31	–	38.67	Fe(II)
	S_4	0.28	–	243.2	14.01	Fe_3C
6	D_1	0.45	0.93	–	45.51	Fe(III)
	D_2	1.07	2.77	–	27.71	Fe(II)
	S_4	0.32	–	247.3	17.39	Fe_3C
	S_2	0.13	–	340.6	9.39	Fe(0)
7	D_1	0.44	0.97	–	47.50	Fe(III)
	D_2	1.08	2.81	–	26.11	Fe(II)
	S_4	0.31	–	247.1	26.49	Fe_3C
8	D_1	0.44	1.01	–	32.30	Fe(III)
	D_2	1.10	2.74	–	19.19	Fe(II)
	S_4	0.30	–	247.9	48.51	Fe_3C
9	D_1	0.46	0.98	–	31.36	Fe(III)
	D_2	1.09	2.81	–	18.83	Fe(II)
	S_4	0.31	–	247.0	49.81	Fe_3C

observations of the composite powders confirm the laser granulometry data (Figs. 3a–3d), and show interesting peculiarities on the macroscopic structure of the growing composite material. Indeed, MWCNTs have grown uniformly and perpendicularly aligned to the entire catalyst grain surface (Figs. 3e, 3g and 3i), with a layer of iron on the top of the CNT mat. This sandwich structure alumina support/CNT mat/catalyst film is clearly visible in Fig. 3i. For long deposition times (>90 min), the general grain fragmentation is confirmed (Figs. 3d and 3f) and CNT growth is entangled (Figs. 3h and 3j). We also noticed the appearance of numerous MWCNT bundles (1–5 µm diameters) that grow from the remaining iron film (see Fig. S1). Moreover, measurements of aligned MWCNT film thickness from SEM micrographs show us that from the beginning of the reaction until the grain fragmentation, the growth rate of the film is constant and consistent with the evolution of grains granulometry (Fig. 2). If the production of aligned CNTs on spherical supports has been recently reported using a floating catalysis process [16–18], to the best of our knowledge the production by FB-CCVD of such composite materials, for which MWCNT length can be easily monitored, is unprecedented.

As the presence of a sandwich structure should be related to an original growth mode of MWCNTs, we have further characterized the catalyst and composite powder all along the synthesis protocol for different deposition times. Characterizations with XRD, SEM, laser granulometry and Mössbauer spectroscopy were systematically conducted. BET specific surface area measurements, FE-SEM, TEM, HRTEM, TGA, and Raman spectroscopy were also performed to complete, when necessary, the characterization.

3.2. Characterization of the fresh OMCVD catalyst

The granulometry of the fresh catalyst and that of the initial support are very similar, and characterized by a mean volume diameter of 322 µm as determined by laser granulometry. The XRD diagram of the fresh catalyst presented in Fig. 4a indicates that different iron crystalline phases are present: (i) hematite (α-Fe_2O_3), (ii) γ-Al_2O_3 and possibly (iii) hercynite ($FeAl_2O_4$) a product resulting from the intercalation of iron inside a network of Al_2O_4. Nonetheless, this latter assignation is uncertain due to the low intensity of the associated diffraction peaks. All the crystalline phases detected by XRD are consistent with the initial support structure (pseudo-Boehmite), the catalyst synthesis oxidative atmosphere and the relatively high temperature of the OMCVD process (575 °C).

Mössbauer spectra (Fig. 5a) of the fresh catalyst at step 1 of the process (Fig. 1a) shows two distinct signals, a doublet D_1 and a sextuplet S_1, whose characteristics are given in Table 2. The dou-

blet has a participation to the signal of 78% and is characteristic of small (5–10 nm) Fe_2O_3 amorphous particles [22]. The sextuplet with a participation to the signal of 22% is also related to a Fe(III) species and is consistent with bulk hematite [23].

SEM observations performed on the fresh catalyst (Figs. 6a–6c) clearly indicate that the active phase is present as a relatively thick (ca. 1 µm, Fig. 6c) surface iron oxide-rich (Fig. 6d) film formed by partially coalesced globular grains of 100 nm to 1 µm (Fig. 6b). Moreover, EDX analysis performed at different levels on a broken grain (Fig. 6a) shows that significant amounts of iron are also present inside the support porosity and that its concentration decreases when going from the surface to the core of the grain. TEM observations (Fig. 7) show that, beside large (0.1–1 µm) aggregates resulting from the presence of the surface thick film (Fig. 7a), small (2–10 nm) nanoparticles are also present in the support porosity (Fig. 7b), in accordance with Mössbauer results. BET measurements give a specific surface area of 150 m^2/g and a porous volume of 0.35 cm^3/g, which is less than those of the boehmite support (204 m^2/g, and 0.5 cm^3/g), indicating that the surface film is discontinuous and that most of the porosity of the support (mean initial pore diameter of 9 nm) is still accessible, just a small part being partially clogged by iron oxide deposition. This latter result implies that some of the iron present in the porosity should be inaccessible.

Thus, in the fresh OMCVD catalyst, iron is present for 20% as a crystalline discontinuous hematite surface film, and for 80% as small (with a diameter under 10 nm) iron oxide amorphous particles located inside the porosity of the γ-alumina. An iron nanoparticles gradient exists between the surface and the core of the alumina grains. As expected, the boehmite support is converted to γ-alumina during the OMCVD process (575 °C) [24].
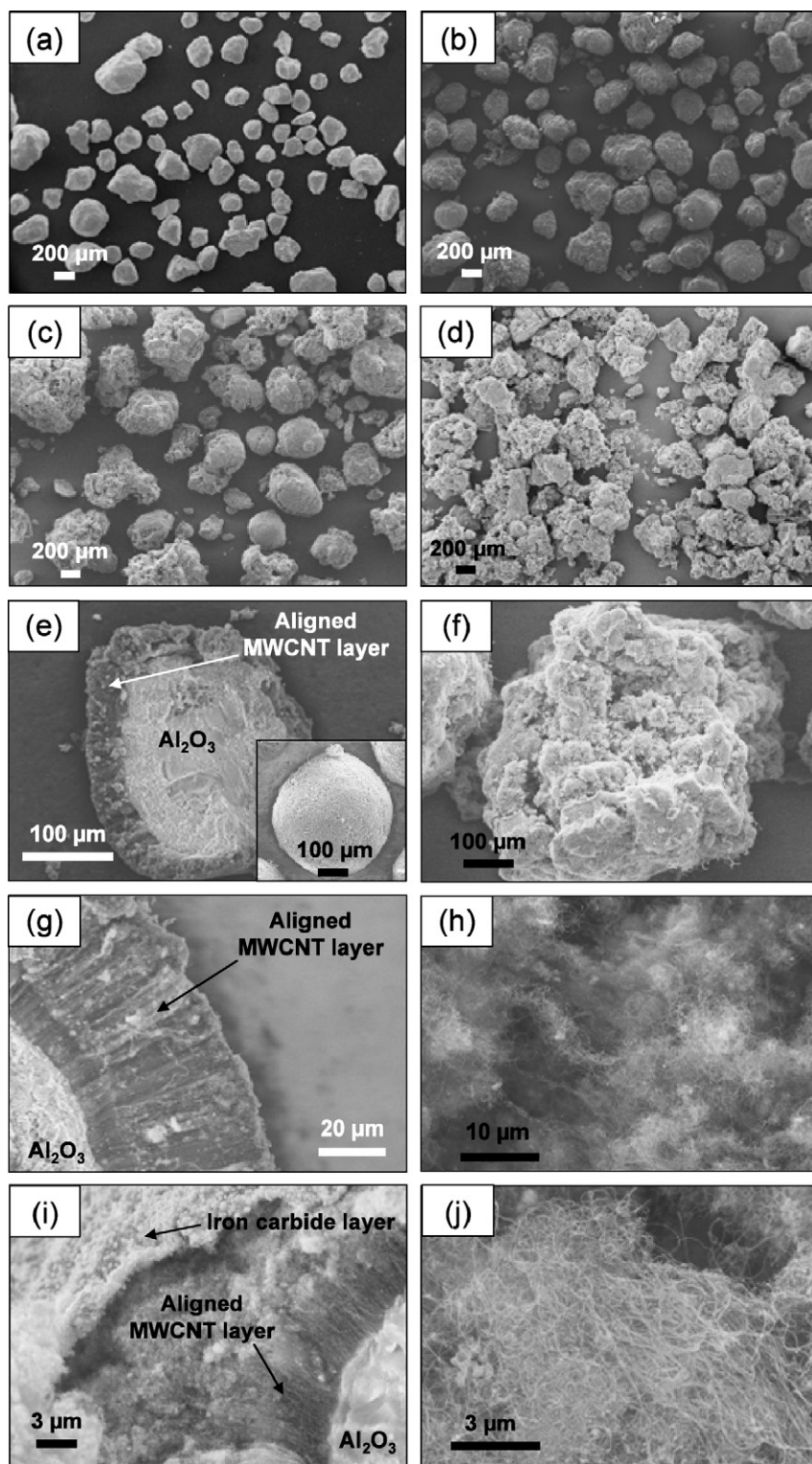
Fig. 3. SEM micrographs of (a) the fresh 10% w/w Fe/Al$_2$O$_3$ catalyst; (b) the composite powder produced after 30 min of reaction; (c) the composite powder after 90 min of reaction; (d) the composite powder after 120 min of reaction; (e) the cross section of an unexploded composite grain; insert into (e) unexploded MWCNT–catalyst composite grain; (f) an exploded composite grain obtained at 120 min of reaction; (g) uniform layer of aligned MWCNTs; (h) entangled MWCNTs produced at long reaction time inside exploded grains; (i) the composite surface obtained at short reaction times showing a layer at the top of the MWCNT mat; and (j) higher magnification of (h).

3.3. Evolution of the catalyst during the heating and reductive steps preceding CNT synthesis

To study catalyst reducibility, the Fe$_2$O$_3$/Al$_2$O$_3$ catalysts were analyzed by temperature programmed reduction experiments. TPR curves (not shown) obtained from Fe$_2O_3$/Al$_2O_3$ samples showed two main reduction steps. The lower temperature peak centered at 380 °C was attributed to reduction of Fe(III) species to Fe$_3$O$_4$, and the second peak, centered at 560 °C was due to reduction of Fe$_3$O$_4$ to FeO and metallic iron [25]. Although a temperature of 650 °C was necessary to completely reduce the catalyst, we decide to perform the reduction step at 400 °C, since it was the
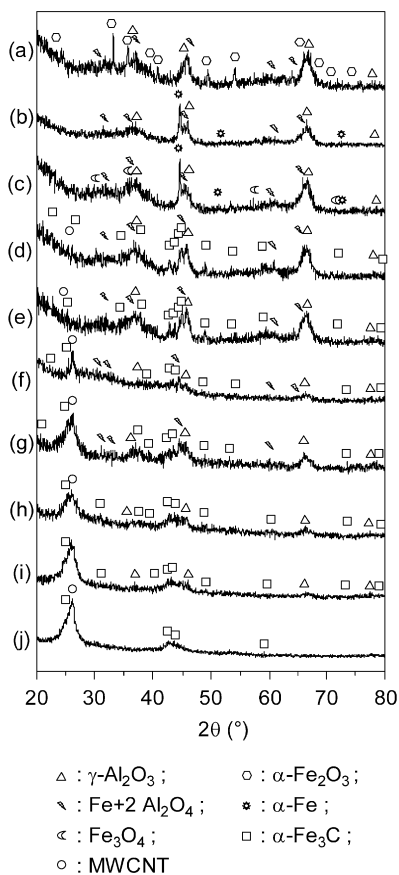
Fig. 4. DRX analysis of the catalyst or of the composite material during the deposit process at: (a) step 1; (b) step 2; (c) step 3; (d) step 4; (e) step 5; (f) step 6; (g) step 7; (h) step 8; (i) step 9; and (j) purified MWCNTs.

Legend:
$\triangle$: γ-Al_2O_3 ; $\circ$: α-Fe_2O_3 ;
$\searrow$: Fe+2 Al_2O_4 ; $\ast$: α-Fe ;
$\ll$: Fe_3O_4 ; $\square$: α-Fe_3C ;
$\circ$: MWCNT

Fig. 5. Mössbauer spectroscopy analysis of the catalyst or of the MWCNT-catalyst composite material during the deposit process at: (a) step 1; (b) step 2; (c) step 3; (d) step 4; (e) step 5; (f) step 6; (g) step 7; and (h) step 8 and step 9.

best compromise between higher temperatures of reduction that induced a complete defluidization of the catalyst bed, due to too high inter-particle forces, and a heating under an inert atmosphere (N_2), which induced lower catalytic performances.

Mössbauer spectrum of the catalyst at step 2 of the process (Fig. 1b), i.e. after the successive heating and reductive steps, is presented in Fig. 5b. It shows three signals: a sextuplet S_2 and two doublets D_1 and D_2. Mössbauer parameters, identification and relative proportion for each signal are listed in Table 2. The D_1 doublet is identical to the one obtained with the fresh catalyst and its participation to the response is lower than for the precedent analysis. This indicates that amorphous Fe_2O_3 nanoparticles are still remaining inside the pores of the support. The S_2 signal corresponds to metallic iron [26] and its proportion, which is quite identical to that of the hematite in the film of the fresh catalyst, leads us proposing that this metallic iron arises from the reduction of the oxide surface film. The D_2 doublet corresponds to iron(II) amorphous species [27], probably FeO, the proportion of which, fits with the "missing" part of Fe(III) nanoparticles of the initial catalyst. Thus, the reductive step leads to a partial reduction of the active phase, which is in agreement with the TPR results and literature data [22] about the hard to reduce behavior of small iron oxide nanoparticles in an Al_2O_3 environment. This phenomenon has been explained by a strong metal–support interaction [22], and in our case probably also by the poor accessibility of part of the active phase. The XRD diagram (Fig. 4b) confirms that α-Fe is present and still indicates the probable presence of hercynite. The absence of hematite diffraction peaks confirms that the metallic iron comes from the initial hematite crystalline surface film. Amorphous FeO and Fe_2O_3 nanoparticles are logically not detected.
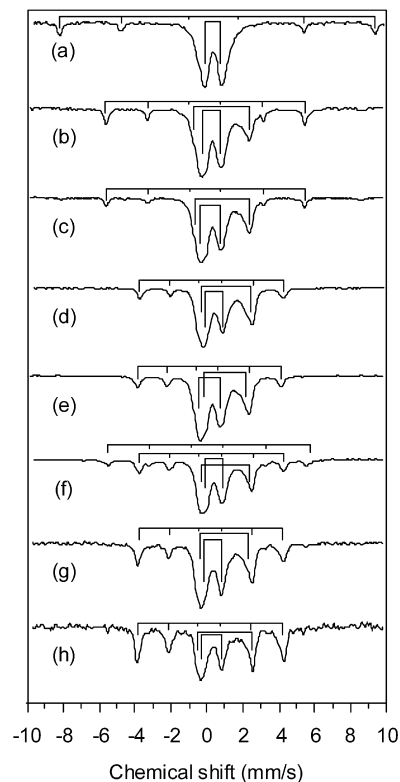
SEM observations of the reduced catalyst (Figs. 6e–6f) show some changes in the textural characteristics of the catalyst. If the surface film remains globally unchanged, particularly its thickness, modifications of its microstructure do appear, with the formation of smaller crystallites and the appearance of fissures and micro-cracks. It is well known that hydrogen reduction of bulk iron oxides produces normally a compact iron layer [25], but if excess hydrogen is present at high temperatures once metallic iron is produced, it will diffuse within and solubilize in the material and stress corrosion cracking and hydrogen embrittlement will occur [28]. Despite extensive study, the mechanism(s) of hydrogen embrittlement and fracture formation is remained unclear [29]. Among the many suggestions, four mechanisms appear to be viable: (i) precipitation of gaseous hydrogen, (ii) formation of hydrides, (iii) deformation localization, and (iv) reduction of cohesion across the grain boundary [30]. The opening of the porosity of the catalyst resulting from hydrogen embrittlement is confirmed by BET measurements that indicate a specific surface area of 160 m^2/g corresponding to a gain of 10 m^2/g.

To summarize the observations made on the catalyst at step 2 of the synthesis route, one can say that the oxide surface film present in the fresh catalyst has been reduced in a metallic α-iron phase with changes in the micro-texture of the surface film, whereas the amorphous Fe_2O_3 oxide nanoparticles present inside the pores of the catalyst remain unreduced or partially reduced to amorphous FeO, probably near the surface of the support for accessibility reasons.

3.4. CNTs-catalyst composite material at the first moments of the synthesis

After the second heating step from 400 to 650 °C under nitrogen (step 3, Fig. 1b), just before ethylene/hydrogen introduction, SEM observations (Figs. 6g and 6h) and BET measurements (a gain
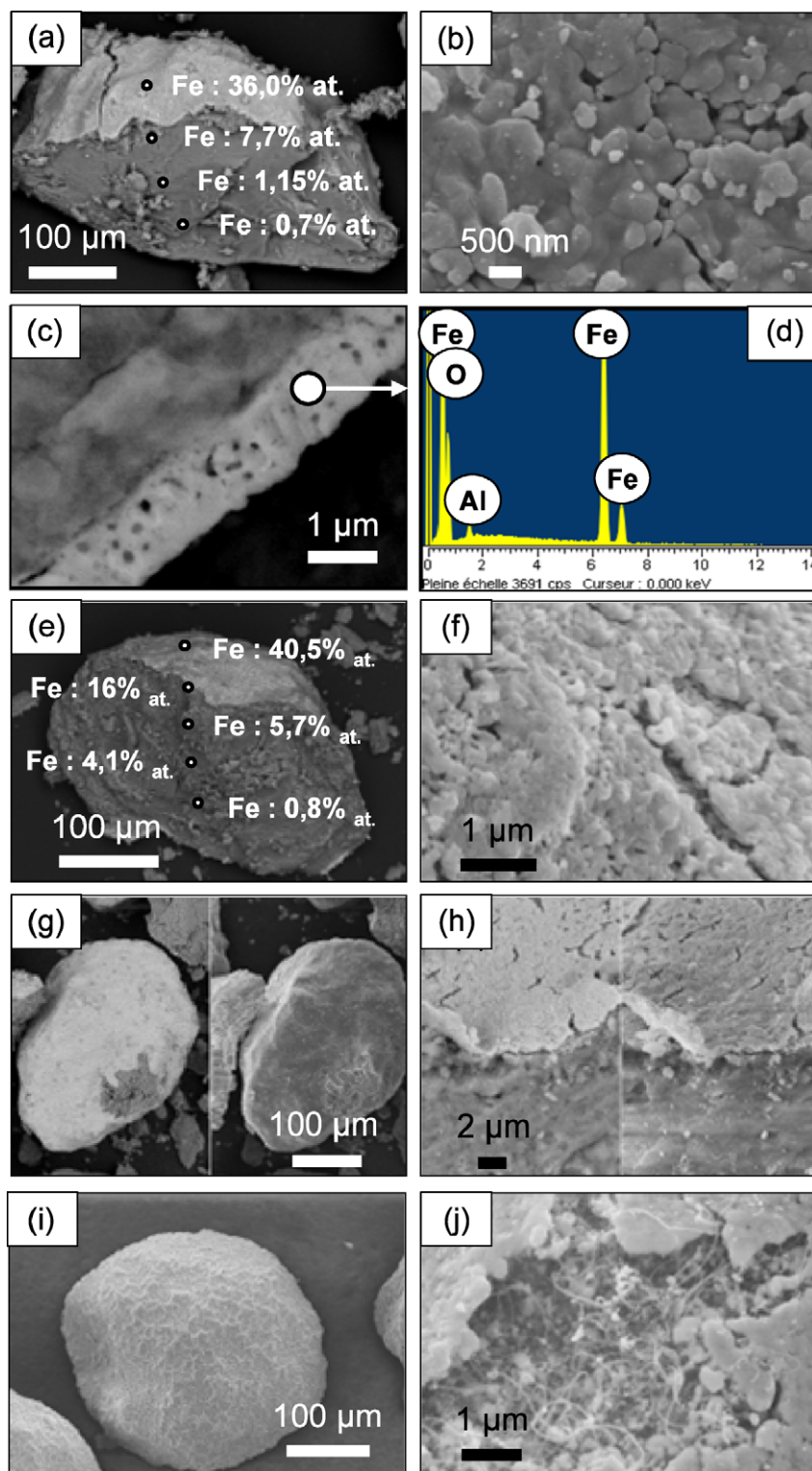
Fig. 6. SEM-EDS observations of (a) to (d) catalyst at step 1 ; (e) and (f) catalyst at step 2; (g) and (h) catalyst at step 3; (i) and (j) MWCNT-catalyst composite material at step 5 (60 s of reaction).

of 2 m^2/g in comparison with the previous step) do not show any change in textural and morphological characteristics of the catalyst. Nonetheless, XRD pattern (Fig. 4c) and Mössbauer spectra and data (Fig. 5c and Table 2) are indicative of chemical composition changes. Indeed, both indicate a partial re-oxidation of the surface crystalline film. XRD indicates the simultaneous presence of magnetite α-Fe$_3$O$_4$ and α-iron, whereas Mössbauer spectra present a new signal, a sextuplet S$_3$, attributed to iron(III) sites

of magnetite [22]. The characteristics of the iron(II) sites of magnetite [22] are very close to those encountered for the doublet D$_2$ of iron(II) amorphous FeO particles. Thus, the large proportions of the D$_2$ signal obtained at step 3 (Table 2) indicate the superposition of these two latter signals. To summarize the Mössbauer and XRD observations, it appears that the second heating under nitrogen leads essentially to a partial re-oxidation of the surface film into magnetite, probably assisted by surface hydroxyl group's
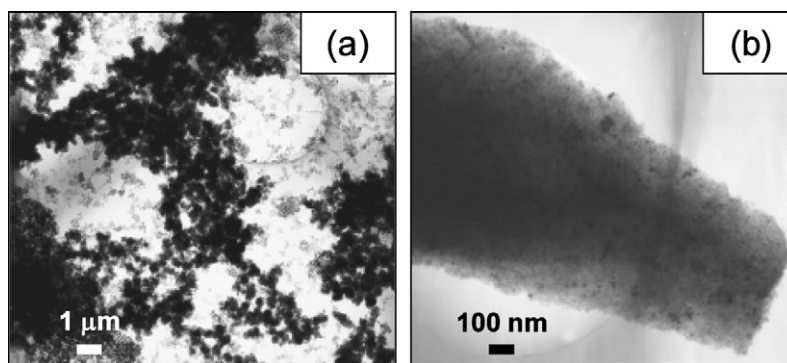
Fig. 7. TEM micrographs showing: (a) the large aggregates of Fe_2O_3 corresponding to the thick film; and (b) small Fe_2O_3 nanoparticles.

decomposition. The high temperature (650 °C), possibly iron catalyzed, dehydroxylation of the support may also impact the surface film adherence, which, in some zones unstuck from the support (Fig. 6h).

During steps 4 and 5 (Fig. 1b), the catalyst has been exposed respectively for a short pulse (approximately 1 s, pulse experiment) and 60 s to the CNT synthesis atmosphere. Mössbauer spectra (Figs. 5d and 5e) are equivalent in terms of responses and relative contribution of each signal. Both show the characteristic doublets D_1 and D_2, respectively, attributed to the small Fe(III) and Fe(II) oxide particles and a new sextuplet S_4 corresponding to cementite (α-Fe_3C) [23]. The contribution of S_4, taking into account that D_1 and D_2 have not significantly changed (Table 2), led undoubtedly to state that the cementite arises from the rapid carburization of the surface metallic film. XRD patterns (Figs. 4d and 4e) confirm the presence of cementite and indicate the formation of a graphitic structure (d_{002} diffraction peak of graphitic material). SEM micrographs (Figs. 6i and 6j) and EDS analysis (not shown) indicate that filamentous carbon is already present even at approximately 1 s of deposition. It is worth mentioning that these carbon filaments seem to grow between the support and the surface film. The microstructure of catalyst grains surface is more and more cracked and damaged, probably due to the formation of filamentous carbon. In order to identify what kind of filamentous carbon is present between approximately 1 and 60 s of reaction, TEM observations have been performed (Fig. 8). First, we can clearly see MWCNTs and significant amount of graphitic carbon/active phase composite structures corresponding to "germs" of CNTs. One can also notice that the density and length of CNTs are logically higher in the 60 s deposit than in the approximately 1 s one. The CNT mean diameter at 60 s reaction is 18.5 nm. At this stage of the process, CNTs are not yet aligned. These micrographs illustrate the necessary and important re-construction step of the surface active phase, which allows producing nucleation and growth sites for MWCNT growth.

These characterizations allow us to state that, during steps 4 and 5 of the process, the catalyst is composed of: (i) a porous alumina core containing Fe (II) and (III) amorphous nanoparticles in the same amounts than at step 3; (ii) a cementite layer resulting from the rapid carburization of the magnetite surface film; and (iii) MWCNTs that grow between the support and the cementite surface film.

3.5. Evolution of the CNTs-catalyst composite material during the 30 to 120 min deposition period

XRD patterns of composite powders obtained at 30 to 120 min of reaction (Figs. 4f and 4i) show the presence of cementite, hercynite, a graphitic material and γ-Al_2O_3. Mössbauer spectra (Figs. 5f and 5h) and data (Table 2) provide additional information. At 30 min of reaction (step 6) and in comparison with the

spectra obtained at 1 min of deposition, the S_4 sextuplet (iron in a cementite environment) and the D_1 doublet (iron in amorphous iron(III) oxide nanoparticles) contributions are stable. The contribution of the D_2 doublet (relative to Fe(II) amorphous nanoparticles) decreases whereas in the same time the signal S_2 of metallic iron reappears. This phenomenon, as well as the evolution of the relative contributions of each signal, is relevant with the complete reduction of a part of the FeO amorphous nanoparticles into metallic iron, these particles being probably the most accessible ones to hydrogen. The fact that no crystalline iron was detected in the XRD pattern can be explained either by the small size of the particles or by X-ray fluorescence emission encountered with the Cu cathode that perturbs the analysis and that conducts to have a signal representative of a 3 to 10 μm layer of the sample [31]. At 60 min of deposition we can see that the intensity of the two doublets D_1 and D_2 has not significantly changed. The sextuplet of metallic iron S_2 has disappeared and the sextuplet S_4 of cementite presents a higher contribution. Thus, the metallic iron nanoparticles have been carburized and the other particles remain inaccessible or not reactive. For longer deposition times, the proportion of iron oxides decreases slowly while that of iron carbide increases. After 90 min of reaction, these proportions remain constant: ~50% of carbide and 50% of oxides.

SEM micrographs of Fig. 9 show typical composite powders produced between 30 and 120 min. At 30 min (Fig. 9a), the aligned MWCNT mat is relatively homogeneous and CNTs grow perpendicularly to the surface grain. Before that, and particularly at 10 min of reaction, the density of CNTs in the mat is not sufficient to obtain aligned CNTs (see Fig. S2).

For a 60 min deposit (Fig. 9b), we can see that some grains have started to fragment because of CNT growth stress, which may occur inside the porosity of the support. It is tempting to correlate this observation with the increase, during the same period, of cementite proportion, arising from the carburization of iron particles present in the porosity of the support. For longer reaction times (Fig. 9c), the fragmentation of catalytic grains is confirmed and generalized. Here also, this is in agreement with the increase of iron carbide proportion measured by Mössbauer spectroscopy between the 60 min and the 90 min deposits. The starting of grain fragmentation between 60 and 90 min of reaction is not accompanied with a decrease of the granulometry of the powder (Fig. 2). Between 90 and 120 min of reaction, although the evolution of grains fragmentation is difficult to follow by microscopy, the granulometry data clearly show that this phenomenon is amplified, and only an entangled MWCNTs growth is observed (Fig. 3c), together with the growth of CNT bundles from the remaining particles present at the surface of the CNT mat (Fig. S1).

It can be seen on the TEM micrograph of the Fig. 8e and the TGA of purified samples (Fig. 8f) that the material produced consists exclusively of MWCNTs (see also Fig. S3). The external mean
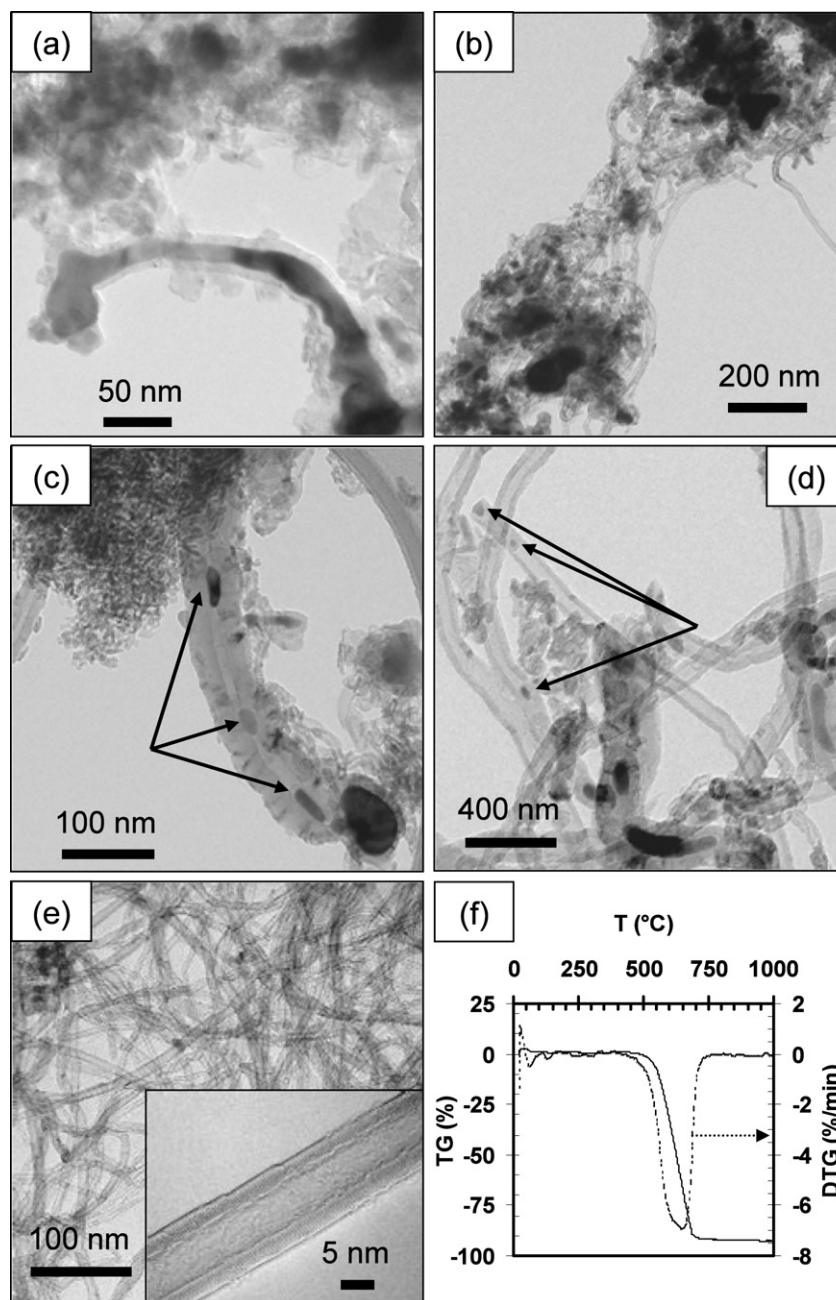
Fig. 8. TEM observations and TGA characterization of MWCNTs: (a) TEM micrograph of restructuring catalyst particle during the growth of a MWCNT at step 4 (approximately 1 s of reaction); (b) to (d) TEM micrographs of the formation of catalyst particles from the catalyst film and "germs" of MWCNTs at step 5 (60 s of reaction); (e) TEM and HRTEM (insert) micrographs of purified MWCNT; and (f) TGA and DTG curves of purified MWCNTs.

diameter of CNTs (Fig. S4) has a tendency to decrease slightly from 30 min reaction (12.2 nm) to 120 min reaction (9.5 nm). This unusual tendency should be linked to the presence of two kinds of catalytic sites for CNT growth. The quality of MWCNTs, which can be assessed from the I_D/I_G ratio on the Raman spectra [32], does not change significantly between 30 and 120 min reaction, since the I_D/I_G ratio oscillates between 0.8 and 1.

3.6. Proposition of a growth mechanism

To go further we propose and discuss an adapted phenomenological growth mechanism deduced from the chemical, morphological and textural specificities of the catalytic system.

The first three steps of the process, including heating and reduction are relatively clear and lead to hydrogen-embrittlement of

the hematite film. The very first moments of CNT synthesis, during which the surface film undergoes remarkable chemical and morphological changes, are particularly interesting. We can explain the heavy surface restructuring by metal dusting, a well-known carburization phenomenon in the steel corrosion field that occurs between 400 and 800 °C in strongly carburizing atmospheres [33], and which leads to the disintegration of metals and alloys into a dust of metal particles and graphite that deposited preferentially on cementite. Thus, this dusting process has already been mentioned to be a source of small particles that could lead to filamentous carbon catalytic growth [34–36]. In our case, the hydrogen-embrittlement of the surface thin film should even enhance the metal dusting phenomenon, which would be responsible for the very fast disintegration of the iron surface film into small cemen-
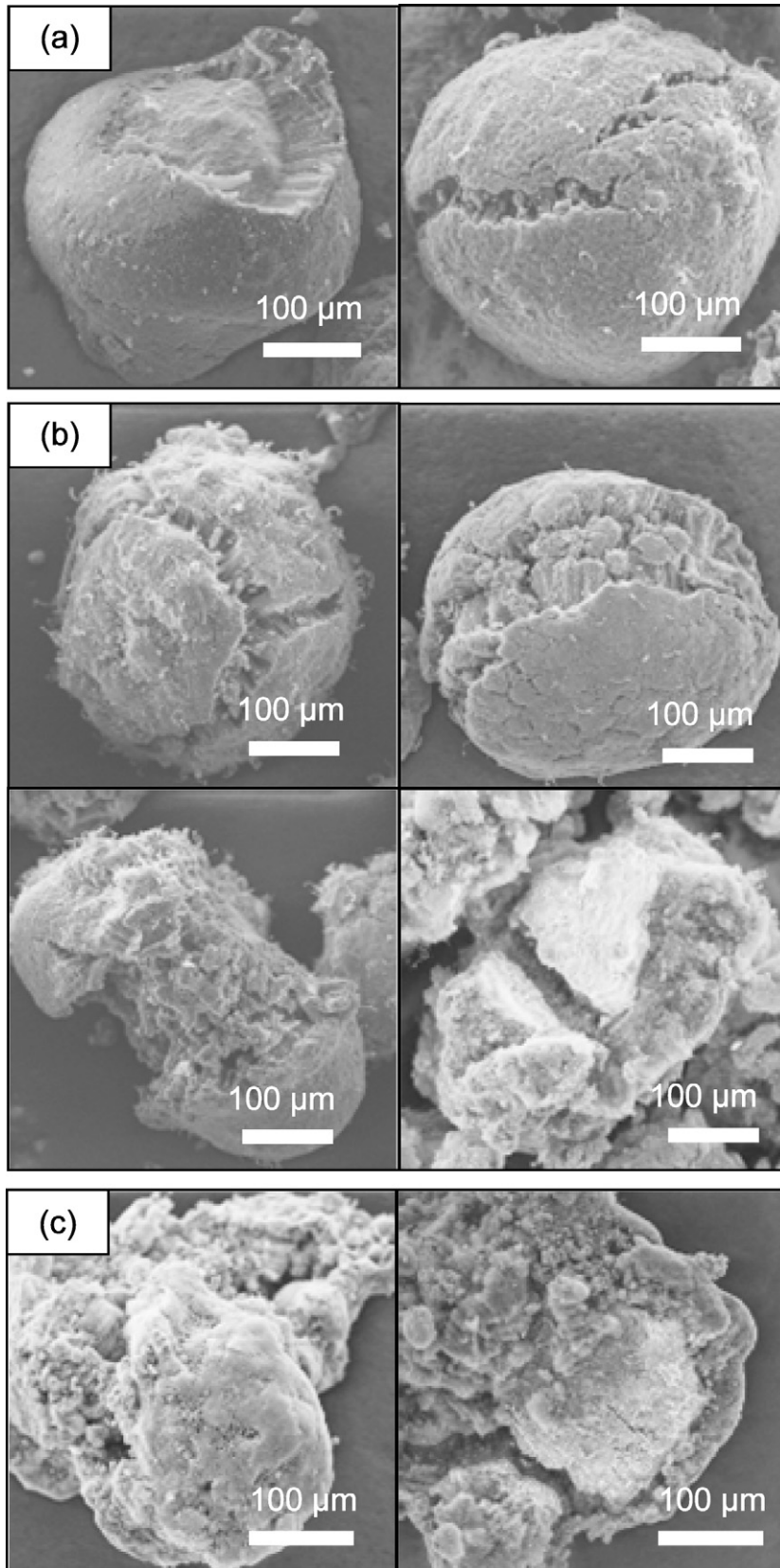
Fig. 9. SEM micrographs of MWCNT-catalyst composite materials grains at: (a) step 6 (30 min deposit); (b) step 7 (60 min deposit); and (c) steps 8 and 9 (90 or 120 min deposit).

tite particles that allow MWCNT nucleation and growth. Indeed, the CNT mean external diameter is fixed after 10 min reaction (see Fig. S4). The larger mean diameter measured at 60 s reaction (18.5 nm) compared to 10 min reaction (11.3 nm) should be due to the incomplete disintegration of the iron surface film into small cementite particles at 1 min reaction.
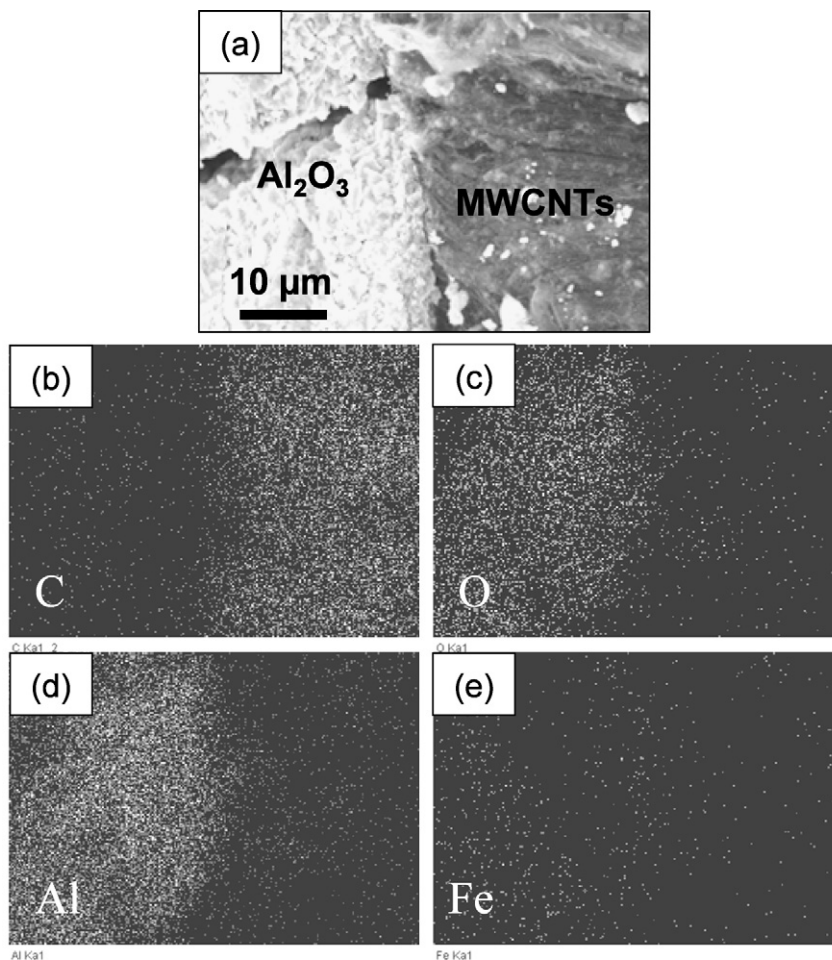
Fig. 10. X-ray cartographies of an aligned MWCNT growth interface: (a) SEM observation of the zone; (b) carbon cartography; (c) oxygen cartography; (d) aluminum cartography; and (e) iron cartography.

The fact that CNT nucleation is located at the bottom of a relatively thick catalyst film is really surprising, and such a growth mode has not yet been reported for aligned MWCNTs. The driving force(s) for this peculiar growth, which implies that one side of the film is more reactive than the other, may originate from:

– The attack of the film by its bottom allowed by the multiples micro-cracks present.
– The existence, at 650 °C, of a temperature gradient between the porous alumina support and the iron phase, which could favor carbon precipitation.
– The poor catalytic surface film/alumina support interaction that causes a low adherence. This latter aspect is generally associated with a "tip-growth" mechanism for carbon nanotubes synthesis [5,6]. From the numerous TEM observations performed on samples prepared between 1 s and 30 min of reaction, we have seen that a particle is very often present at the closed tip of CNTs (see Fig. S5), thus confirming the "tip-growth" mechanism from the catalytic surface film.

This original growth mode points out the importance of the metal–support interface for CNT synthesis. Interestingly a bottom-up growth of CNT multilayer has been reported, where each new layer of aligned CNTs nucleates and grows from the original substrate surface at the bottom of the existing multiple stacks of nanotubes, the preexisting multiple nanotube stacks lifting up to accommodate the vertical growth of fresh layers [37].

After this first nucleation step from the primary catalytic sites, a uniform growth of CNTs takes place from the nucleated germs, between the support and the uprising active phase layer. The CNTs start to align, due to their high density after 10 min of reaction. The alignment of MWCNTs is classically explained in terms of high particles density [38] that permits the orientation during the growth and self-upstanding of the MWCNTs forest. This explanation however is not completely satisfactory and too simplified, since experiments (not shown) conducted at other temperatures (550, 600, 700 and 750 °C) [39] indicate that the alignment disappears above 650 °C. We can refine the classical explanation by mentioning the necessity to obtain a correct balance between the rates of two phenomena: the dusting at the origin of CNT nucleation sites and carbon diffusion/precipitation that contributes to CNT formation. An increase of temperature might provoke an unbalance that leads to entangled MWCNT growth.

The original growth reported herein leads to regular consumption of the iron film. Fig. 10 shows X-ray cartographies of an aligned MWCNT mat interface that confirms the presence of iron all along the growing CNT layer. This observation fits well with our explanation. The catalytic cementite film consumption, resulting in loss of active metal during the process could be due either to further particle disintegration or to capillarity forces that allow the encapsulation of "molten" metal particles into the CNT inner cavity (see Figs. 8c and 8d). Another explanation could involve a metastable equilibrium existing between cementite and graphitic carbon [40], which leads to the liberation of α-iron (stable phase in the presence of graphitic carbon) encapsulated inside the grow-
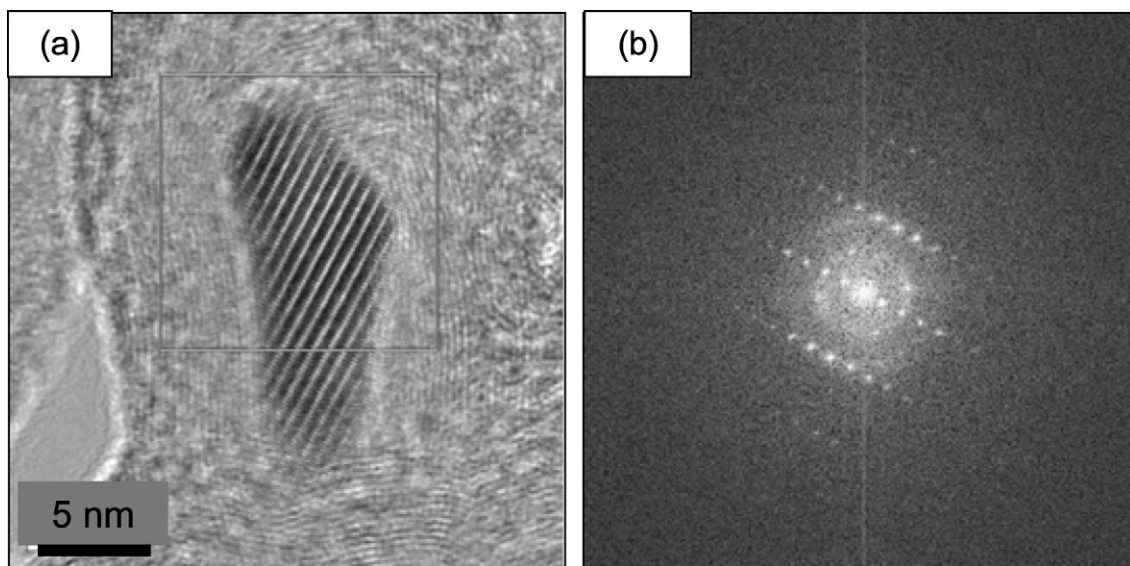
Fig. 11. (a) HRTEM observation of a particle encapsulated inside a MWCNT, and (b) 2D fast Fourier transform (2D-FFT) of the area indicated with a square in (a).

ing nanotube. Thus, the concomitant presence of metallic iron and of Fe_3C particles in MWCNTs has been recently reported [41]. In order to elucidate the chemical nature of CNT encapsulated iron particles, HRTEM observations (Fig. 11) have been performed. The analysis of HRTEM data allows to completely ruling out that the particle is constituted by metallic iron. Besides, the comparison with different and well known iron carbide crystalline structures, permits to indicate the orthorhombic Fe_3C—oriented in its $\langle 120 \rangle$ zone axis—as the most probable crystalline structure that should constitute the nanoparticle embedded in the MWCNT structure. However, in such a determination, some concomitant elements of uncertainty are present and have to be taken into account. They arise from (i) the very low difference between the d-values of different sets of lattice plans, that often is of the same order of the intrinsic uncertainty of the d-values as measured by 2D-FFT analyses. This makes very difficult a completely doubtless determination of the exact composition of the iron carbide on the base of the only measured structural parameters, even considering that the structural parameters are strongly dependent on the amount of iron and carbon in iron carbide; and (ii) the presence of CNT walls that may induce an external stress on the particles and thus give rise to lattice parameters changes with respect to those known for the iron carbide bulk phases.

Finally, it is also worth noting that, when the CNT mat has stopped growing, i.e. during the last 30 min of reaction, long (50–100 μm) bundles of MWCNTs are present on the top of the mat from the last relatively large particles arising from the film consumption (see Fig. S1).

The active surface film being consumed with the growth of aligned CNTs from ethylene, the synthesis hydrogen rich atmosphere should reach more and more easily the core of the grain to slowly reduce the hard to reduce and well dispersed nanoparticles located inside the porosity of the alumina support. These newly active particles, in strong interaction with the support, will be then carburized, and allow the appearance of "secondary" growth sites for MWCNTs. This will induce a progressive fragmentation of the catalytic grains under the constraints of "secondary" growing CNTs. It is interesting to underline that this growth mode with successive liberations and activation of active sites by fragmentation of the growing grains reminds precisely the one encountered with Ziegler–Natta heterogeneous catalysis to obtain under certain conditions polymers from α-olefins [42]. During this period that involves the availability of "new" Fe_3C, the catalytic activity increases
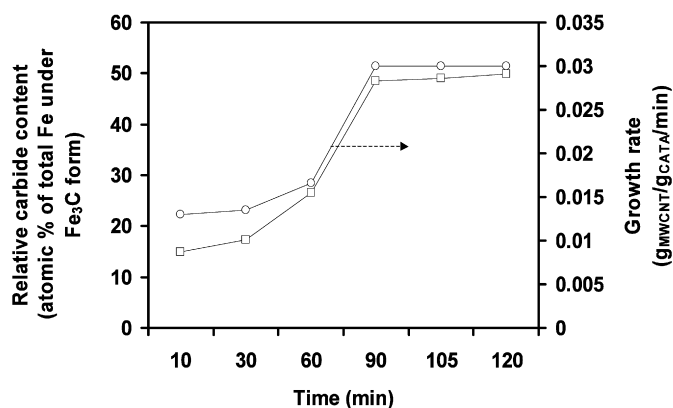

Fig. 12. Growth rate (right) and relative carbide content (left) plotted versus time of reaction.

significantly. From Fig. 12, which shows a nice correlation between the percentage of Fe_3C and the catalytic activity, we can conclude that CNT germination, either from the primary (film) or secondary (nanoparticles) catalytic sites, stands for 90 min of reaction. Of course, there might be a moment where the two growth (primary aligned and secondary entangled) modes occur concomitantly. The CNT growth on the "secondary" catalytic sites, i.e. the hard to reduce nanoparticles in strong interaction with the alumina support, seems to follow a "base-growth" mechanism. Indeed, from the numerous TEM observations performed on samples grown between 90 and 120 min (see Fig. S6), it appears that the proportion of CNTs without nanoparticles at their tip is very important compared to the samples grown between 1 and 30 min of reaction (see Fig. S5). The absence of catalyst nanoparticle at the tip of CNTs is in accordance with a strong metal–support interaction [5]. Interestingly, the external mean diameter of CNTs grown from the catalyst film (large globular grains disintegrated by metal dusting) and from the small nanoparticles in strong interaction with the support are relatively similar (see Fig. S4), even if the former are slightly larger. We have not yet a satisfactory explanation of this result.

The existence of two distinct growth regimes, one from the surface film and the other from hard to reduce particles located in the porosity of the alumina has been confirmed by kinetic data [20]. Indeed, a low apparent activation energy for CNT formation of 29 kJ/mol has been obtained from the initial times of synthe-
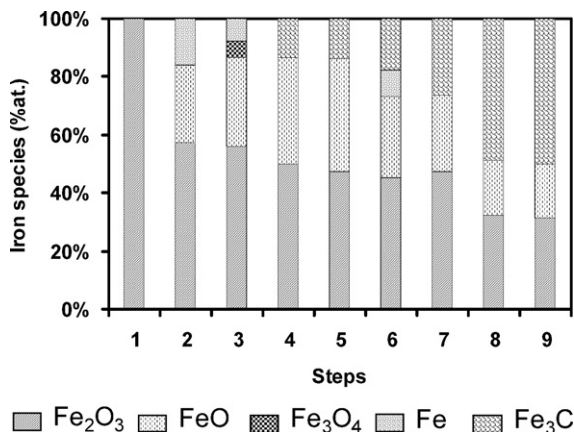
Fig. 13. Evolution of iron species atomic proportions during the different MWCNT synthesis steps.

Fig. 14. Schematic evolution of the characteristic catalyst and catalyst-MWCNT composite material structures during the synthesis process: (a) step 1; (b) step 2; (c) step 3; (d) steps 4 and 5; (e) step 6; (f) and (g) steps 7 to 9.

sis (from the surface film), whereas a significantly higher value of 120 kJ/mol has been calculated from the activity at 40 min of run (from both surface film and entrapped nanoparticles). Thus, for this catalyst the mechanisms of nucleation and to a lesser extent growth of CNTs require low activation energy for the catalyst film, and a higher one for the iron particles in strong interaction with the alumina support. The first activation energy of 29 kJ/mol is significantly lower than the activation energy reported for C diffusion in α-iron (67 kJ/mol) [43], and could correspond to a surface carbon diffusion for the tip growth mechanism. The second activation energy is closer to the activation energy of carbon diffusion in γ-iron (142 kJ/mol) [43]. This could indicate first that for small diameter nanoparticles in strong interaction with the substrate, phase transition occurs at relatively low temperatures (650 °C) from α-iron to γ-iron. A method of synthesizing stable γ-Fe selectively inside a carbon nanotube by transforming α-Fe through electron irradiation in situ inside a transmission electron microscope has been recently reported [44]. Second, from these small particles, bulk carbon diffusion and a base-growth mechanism prevails.

In order to summarize the results of catalyst characterization all along the process, we plotted the evolution of the nature of the iron species (Mössbauer data) along the different steps (Fig. 13), and schematized the localization of the different iron phases (Fig. 14).

- Step 1: the catalyst is composed of 20% of Fe_2O_3 as a crystalline surface film and 80% of <10 nm Fe(III) particles in strong interaction with the alumina support.
- Step 2: after the reductive step at 400 °C: (i) the Fe_2O_3 surface film is reduced to metallic α-iron and undergoes a severe reconstruction due to hydrogen embrittlement; and (ii) part of the hard to reduce Fe(III) particles are reduced into FeO.
- Step 3: the heating to 650 °C under nitrogen induces a partial re-oxidation of the surface film to magnetite, probably due to reaction with surface hydroxyl groups.
- Steps 4 and 5: with the introduction of C_2H_4 and H_2 the surface film is completely carburized after 1 min of reaction and CNT growth starts instantaneously between the surface film and the support.
- Step 6: A controllable and linear growth of an aligned MWCNTs (10–12 nm ext. diameters) mat around the catalyst grain is observed between 10 and 30 min of reaction, accompanied with a progressive consumption of the surface film.
- Step 7: Between 30 and 60 min of reaction a second growth regime appears, the CNTs growing in an entangled manner
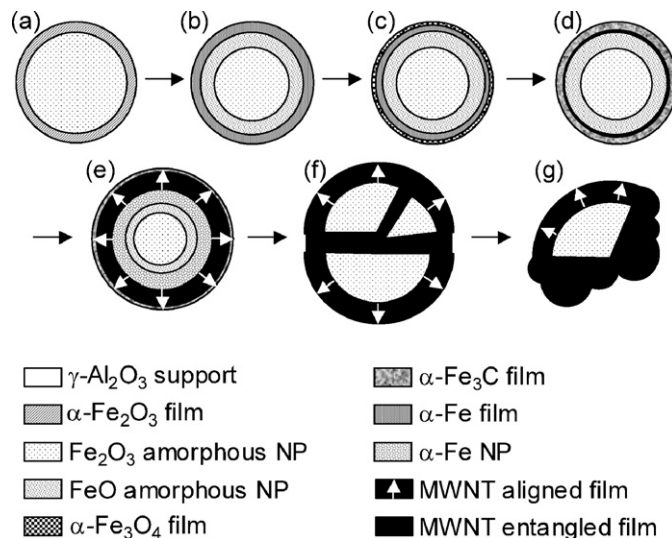
from particles located inside the porosity of the support with a concomitant fragmentation of the catalyst grains.
- Steps 8 and 9: At 90 min of reaction, the grain fragmentation is generalized and part of the previously inactive Fe(II) and Fe(III) particles are activated into cementite. Between 30 and 90 min reaction, the CNT mat continues to grow, to reach a plateau corresponding to 75 μm at 90 min reaction. Between 90 and 120 min reaction no significant evolution of the nature of the iron species was noticed, and the reaction rate remains constant, meaning that during this period mainly CNT growth occurs. During the last thirty minutes of reaction, the grain fragmentation continues, inducing a significant decrease of the granulometry of the composite powder.

4. Conclusion

The characterization of the alumina supported iron system at different steps of MWCNT synthesis allowed us to propose a phenomenological nucleation and growth mechanism for CNTs. First, MWCNTs are produced on the whole surface of the catalyst from a cementite surface film. The regular consumption of the catalytic film results in high CNTs density, which grow vertically aligned to the surface of the catalyst grains. Between 30 and 60 min of reaction, entangled MWCNT growth appeared from secondary catalytic sites, constituted by small nanoparticles located in the porosity of the support and in strong interaction with this latter. This second growth is accompanied by the fragmentation of the catalyst grains. To the best of our knowledge, several aspects of this MWCNT growth mode are unprecedented: (i) the high activity of a relatively thick (1 μm) surface film for aligned MWCNT growth. Indeed, it is generally accepted that nanometric thick films should be used to grow vertically aligned CNTs [45,46]; (ii) the nucleation and aligned growth of MWCNTs from large particles; and (iii) the aligned growth of CNTs between the surface film and the support, and the consumption of the film. The possibility to synthesize at large scale aligned MWCNTs is then opened.

References

[1] P.M. Ajayan, Chem. Rev. 99 (1999) 1797.

[2] H.J. Dai, Acc. Chem. Res. 35 (2002) 1045.

[3] M. Monthioux, P. Serp, E. Flahaut, C. Laurent, A. Peigney, M. Razafinimanana, W. Bacsa, J.-M. Broto, in: B. Bhushan (Ed.), Handbook of Nanotechnology, Springer, Berlin, 2004, p. 39.

[4] R. Philippe, A. Morançais, M. Corrias, B. Caussat, Y. Kihn, P. Kalck, D. Plee, P. Gaillard, D. Bernard, P. Serp, Chem. Vap. Deposition 13 (2007) 447.

[5] A.-C. Dupuis, Prog. Mater. Sci. 50 (2005) 929.

[6] R.T.K. Baker, Carbon 27 (1989) 315.

[7] P.J.F. Harris, Carbon 45 (2007) 229.

[8] C. Ducat, I. Alexandrou, M. Chlowalla, J. Appl. Phys. 92 (2002) 3299.

[9] R.T.K. Baker, P.S. Harris, R.B. Thomas, J. Waite, J. Catal. 30 (1973) 86.

[10] A. Gohier, C.P. Ewels, T.M. Minea, M.A. Djouadi, Carbon 46 (2008) 1331.

[11] H. Ago, T. Komatsu, S. Ohshima, Y. Kuriki, M. Yumura, Appl. Phys. Lett. 77 (2000) 79.

[12] M. Perez Cabero, E. Romeo, C. Royo, A. Monzon, A. Guerrero-Ruiz, I. Rodriguez-Ramos, J. Catal. 224 (2004) 197.

[13] W.Z. Li, S.S. Xie, L.X. Qian, B.H. Chang, B.S. Zou, W.Y. Zhou, R.A. Zhao, G. Wang, Science 274 (1996) 1701.

[14] G.S. Choi, K.H. Son, D.J. Kim, Microelectron. Eng. 66 (2003) 206.

[15] I. Janowska, G. Winé, M.-J. Ledoux, C. Pham-Huu, J. Mol. Catal. A 267 (2007) 92.

[16] R. Xiang, G. Luo, W. Qian, Y. Wang, F. Wei, Q. Li, Chem. Vap. Deposition 13 (2007) 533.

[17] Q. Zhang, J.-Q. Huang, M.-Q. Zhao, W. Qian, Y. Wang, F. Wei, Carbon 46 (2008) 1152.

[18] R. Xiang, G. Luo, Z. Yang, Q. Zhang, W. Qian, F. Wei, Mater. Lett. 63 (2009) 84.

[19] D. Plee, R. Philippe, B. Caussat, P. Kalck, P. Serp, French Patent WO2008107586.

[20] R. Philippe, P. Serp, P. Kalck, Y. Kihn, D. Plee, P. Gaillard, D. Bernard, B. Caussat, AIChE J. 55 (2009) 450.

[21] A. Morançais, B. Caussat, Y. Kihn, P. Kalck, D. Plee, P. Gaillard, D. Bernard, P. Serp, Carbon 45 (2007) 624.

[22] F. Arena, G. Gatti, G. Martra, S. Coluccia, L. Stievano, L. Spadaro, P. Famulari, A. Parmaliana, J. Catal. 231 (2005) 365.

[23] N.N. Greenwood, T.C. Gibb, Mössbauer Spectroscopy, Chapman and Hall, London, 1971.

[24] G. Paglia, C.E. Buckley, A.L. Rohl, R.D. Hart, K. Winter, A.J. Studer, B.A. Hunter, J.V. Hanna, Chem. Mater. 16 (2004) 220.

[25] A. Pineau, N. Kanari, I. Gaballah, Thermochim. Acta 447 (2006) 89.

[26] I.V. Murin, V.M. Smirnov, G.P. Voronkov, V.G. Semenov, V.G. Povarov, B.M. Sinel'nikov, Solid State Ionics 133 (2000) 203.

[27] N. He, Y. Kuang, Q. Dai, Y. Miao, A. Zhang, X. Wang, K. Song, Z. Lu, C. Yuan, Mater. Sci. Eng. 9 (1999) 151.

[28] M.E. Stroe, Ph.D. thesis, Brussels free University, 2005.

[29] G.V. Karpenko, A.K. Litvin, V.I. Tkachev, A.I. Soshko, Mater. Sci. 9 (1975) 367.

[30] L. Zhong, R. Wu, A.J. Freeman, G.B. Olson, Phys. Rev. B 62 (2000) 13938.

[31] C. Hammond, in: Smithells Metals Reference Book, 8th ed., X-Ray Analysis of Metallic Materials, Butterworth, Stoneham, MA, 2004.

[32] H. Yan, Q. Li, J. Zhang, Z. Liu, Carbon 40 (2002) 2693.

[33] P. Szakalos, Mater. Corros. 54 (2003) 752.

[34] B. Schmid, N. Aas, Ø. Grong, R. Ødegård, Appl. Catal. A Gen. 215 (2001) 257.

[35] C.Y. Lin, W.T. Tsai, Mater. Chem. Phys. 82 (2003) 929.

[36] Z. Zeng, K. Natesan, Chem. Mater. 17 (2005) 3794.

[37] X. Li, A. Cao, Y.-J. Jung, R. Vajtai, P.M. Ajayan, Nano Lett. 5 (2005) 1997.

[38] S. Fan, M.G. Chapline, N.R. Franklin, T.W. Tombler, A.M. Cassell, H. Dai, Science 283 (1999) 512.

[39] R. Philippe, Ph.D. thesis, INPT, 2006.

[40] H. Kim, W. Sigmund, J. Cryst. Growth 276 (2005) 594.

[41] H. Kim, W. Sigmund, Carbon 43 (2005) 1743.

[42] A. Muñoz-Escalona, A. Parada, J. Cryst. Growth 48 (1980) 250.

[43] P. Serp, in: P. Serp, J.L. Figueiredo (Eds.), Carbon Materials for Catalysis, Wiley, Hoboken/New Jersey, 2009.

[44] H. Kim, M.J. Kaufman, W.M. Sigmund, J. Mater. Res. 19 (2004) 1835.

[45] G. Eres, A.A. Puretzky, D.B. Geohegan, H. Cui, Appl. Phys. Lett. 84 (2004) 1759.

[46] H.T. Ng, B. Chen, J.E. Koehne, A.M. Cassell, J. Li, J. Han, M. Meyyappan, J. Phys. Chem. B 107 (2003) 8484.